Aerospace Science and Technology 168 (2026) 110775

Contents lists available at ScienceDirect

Aerospace Science and Technology

journal homepage: www.elsevier.com/locate/aescte

Original article

Analysis of separation control mechanism of turbulent co-flow wall jet

Kewei Xu [a,*], Yan Ren [b], Gecheng Zha [b]

[a] Department of Mechanical Engineering, University of Maine, Orono, ME 04469, United States of America
[b] Department of Mechanical and Aerospace Engineering, University of Miami, FL 33124, United States of America

ARTICLE INFO

Communicated by Qiulin Qu

Keywords:
Co-flow wall jet (CFJ)
Active flow control (AFC)
Turbulent wall jet momentum equation
Separation control mechanism
Adverse pressure gradient

ABSTRACT

Utilizing an upstream tangential injection and downstream streamwise suction, co-flow wall jet (CFWJ) is demonstrated to be an effective and efficient zero-net-mass-flux active flow control method. However, the underlying separation control mechanism is not fully understood. This paper conducts a theoretical analysis using two-dimensional (2D) differential and integral wall jet momentum equations, which are supported by quantitative solutions of 2D unsteady Reynolds averaged Navier-Stokes equations for the NASA hump flows. This study reveals the CFWJ working mechanism with three factors: 1) A CFWJ establishes the required large clockwise spanwise vorticity and transverse gradient of vorticity magnitude near the wall by tangential injection and streamwise suction. This is essential to offset the adverse pressure gradient (APG) by enhancing the turbulent diffusion and the wall vorticity flux. 2) The wall jet provides the required streamwise mass flux to enhance the streamwise inertia force that offsets the APG. 3) The turbulent diffusion is enhanced by the severe APG, which in turn counteracts the effect of APG. The validated numerical simulation demonstrates that turbulent diffusion plays a dominant role in offsetting APG. It is observed that immersing the entire CFWJ in the APG region is most effective and efficient for flow separation control.

1. Introduction

Active Flow Control (AFC) has the potential to break through conventional fluid mechanics limitations and provides significant performance improvement to fluid systems [1]. AFC is to transfer external energy to the controlled flows in order to improve the performance of the flow systems. Since flow separation was first addressed by Prandtl [2], separation control has been an important application area of AFC.

Synthetic jets [3,4] generated by periodic motion of a piston or diaphragm and plasma jets [5,6] based on plasma discharge are zero-net-mass-flux (ZNMF) flow controls, which require no external flow source. However, the actuators of these methods have low energy conversion efficiency of less than 10% [7]. Co-flow Wall Jet (CFWJ) is a recently developed ZNMF active flow control method, which has high effectiveness in lift enhancement [8,9], flow distortion control [10], separation removal [7], etc, and high energy conversion efficiency [11]. As sketched in Fig. 1, CFWJ has a streamwise suction drawing a small amount of mass flow in the downstream, pressurizes and energizes the mass flow using a micro-compressor actuator system embedded inside, and then tangentially injects the same amount of mass flow in the upstream.

Since the co-flow wall jet belongs to the wall jet family, it is worthwhile to briefly review the wall jet study for providing the overall background. Launder and Rodi [12] define a wall jet as a "boundary layer in which, by virtue of the initially supplied momentum, the velocity over some region in the shear layer exceeds that in the free stream". Apart from the co-flow wall jet, wall jets are widely used for the circulation control airfoil [13–15] and aircraft upper surface blowing [16–19]. There is a rich literature on wall jet studies pioneered by Forthmann with his first paper on wall jet in 1936 [20]. There are multiple wall jet studies after, including the important contributions of Glauert [21], Launder and Rodi [12], Bradshaw and Gee [22], Newman et al. [23], Wygnanski et al. [24], Dairay et al. [25], Guo et al. [26] and Gupta et al. [27]. Most of these studies are focused on understanding the fundamental physics behaviors of the wall jets, either with or without external streams, such as the velocity scaling law, skin friction, eddy viscosity and shear stress distribution, shear layer growth rate, forced excitation, transition, jet impingement, etc. A few studies address the wall jet mechanism for separation control, even though it is well recognized that the wall jet is effective in suppressing flow separation due to energizing the boundary layer.

* Corresponding author.
E-mail address: kewei.xu@maine.edu (K. Xu).

https://doi.org/10.1016/j.ast.2025.110775
Received 16 April 2025; Received in revised form 14 July 2025; Accepted 11 August 2025

Available online 19 August 2025

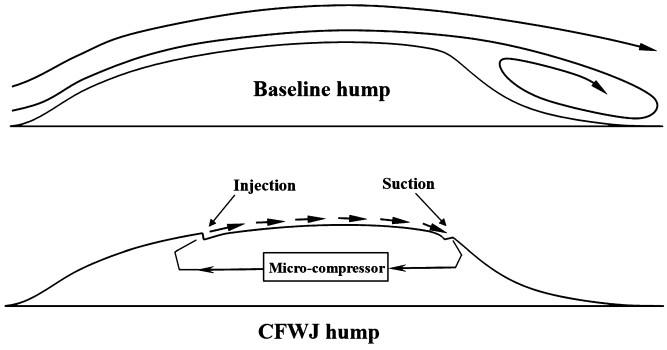

Fig. 1. Sketches of the baseline NASA hump (Top) and CFWJ hump (bottom).

Although "energizing the boundary layer" seems to be a general understanding as the course that makes the flow attached, there is no clear knowledge of what factor plays the key role in "energizing the boundary layer" to overcome the adverse pressure gradient. Therefore, it is important to break down the terms in the wall jet question to examine each term and its role. The purpose of this paper is to study CFWJ.

In CFWJ, the ejected turbulent wall jet will destabilize the main flow and trigger the main flow to become turbulent. The streamwise suction has a non-90° angle with the local wall surface that increases not only the transverse momentum of the flow but also the streamwise momentum. Our prior work [7] studied the CFWJ's energy efficiency. It indicates that it is most effective and efficient to place the injection slightly downstream of the separation onset location and immerse the entire CFWJ in adverse pressure gradient region. Following the study of the energy expenditure of CFWJ [7], it is important to ask a further question: why is CFWJ able to overcome the adverse pressure gradient and make the flow attached? This is also motivated by many other previous works where CFWJ airfoil can sustain an extreme adverse pressure gradient (EAPG) [28] at 65° of angle of attack (AoA) and achieve a C_{Lmax} exceeding the theoretical limit of potential flow [29], $C_{Lmax} = 2\pi(1 + t/c)$ in both experiments and numerical simulations [30,31]. Apart from our work, the effectiveness of CFJ is also reported by other research groups [32–35].

To answer the above question, the wall jet momentum equation is studied in this paper. The effects of injection and suction on flow attachment are evaluated using the 2D URANS simulation. Although the turbulent wall jet momentum equation is well known, the research to analyze and understand the separation control mechanism for CFWJ is the first time. The outcomes of the present study not only apply to the CFWJ but are extendable to the general wall jet AFC. The present paper is an extension of the CFWJ energy-expenditure study [7] and is refined based on the previous conference publication [36].

2. Separation control analysis based on turbulent wall jet momentum equations

The proposed analysis framework for separation control based on the two forms of the turbulent wall jet momentum equation is briefly discussed below.

2.1. Differential form

Assuming negligible body forces, the normalized two-dimensional incompressible turbulent wall jet momentum equation in the x-direction can be approximated as follows. Here, x denotes the direction tangential to the wall surface (pointing downstream), and y is the direction normal to the wall (pointing outward). The velocity components in the x and y directions are denoted by u and v, respectively. The dynamic viscosity (μ) includes molecular viscosity (μ_m) and turbulent viscosity (μ_t). Note that the dimensional terms are normalized following $\bar{u} = u/u_\infty$, $\bar{x} = x/L_\infty$, $\bar{y} = y/L_\infty$, $\bar{\mu} = \mu/\mu_\infty$, $\bar{p} = p/(\rho_\infty u_\infty^2)$ and $\bar{\rho} = \rho/\rho_\infty$, and that after normalization over-lines are omitted for simplicity.

$$\rho u\frac{\partial u}{\partial x} + \rho v\frac{\partial u}{\partial y} - \frac{1}{Re}\frac{\partial \mu}{\partial y}\frac{\partial u}{\partial y} + \frac{\partial p}{\partial x} = \frac{\mu}{Re}\frac{\partial^2 u}{\partial y^2} \tag{1}$$

The first two terms on the left-hand side (LHS) of Eq. (1) are the convective terms, which are responsible for transporting the wall jet momentum in streamwise and transverse (normal wall) directions. The third term represents the turbulence diffusion due to the turbulent eddy viscosity gradient. This term is negligible for laminar flow since the viscosity coefficient is fairly constant, but is shown to be dominant in the present study for turbulent wall jet mixing due to the rapidly growing rate of turbulent eddy viscosity near the wall.

On the right-hand side (RHS) of Eq. (1), the term $\partial^2 u/\partial y^2$ is an indicator of the flow status away from the wall. A negative value indicates a convex velocity profile as an attached flow, and a positive value indicates a concave velocity profile, meaning flow separation. More discussions regarding how the sign of $\partial^2 u/\partial y^2$ is related with flow status can be referred to Ref. [1,36,37]. In adverse pressure gradient, the term $\partial p/\partial x$ is positive.

The current mechanism analysis is to see how the first three terms (representing different effects of flow control) are enhanced by CFWJ to offset the positive $\partial p/\partial x$ and drive the RHS $\partial^2 u/\partial y^2$ to negative for flow attachment. To do this, the first three terms are quantified through a validated 2D URANS simulation, which provides direct insights into their respective contribution to the flow attachment.

For the tangential injection of co-flow wall jet, Eq. (1) can be also expressed in terms of spanwise vorticity as:

$$\omega_z = \frac{\partial v}{\partial x} - \frac{\partial u}{\partial y} \approx -\frac{\partial u}{\partial y} \tag{2}$$

This is because the jet ejected tangentially to the wall has $\partial v/\partial x << \partial u/\partial y$. The wall jet momentum Eq. (1) downstream of the injection slot may be rewritten as:

$$\rho u\frac{\partial u}{\partial x} - \rho v\omega_z + \frac{\omega_z}{Re}\frac{\partial \mu}{\partial y} + \frac{\partial p}{\partial x} \approx -\frac{\mu}{Re}\frac{\partial \omega_z}{\partial y} \tag{3}$$

The second term in Eq. (3) represents the vorticity flux. The vorticity form of the equation will facilitate the understanding of vorticity convection effect in later discussion.

2.2. Integral form

The lump effect can be obtained by integrating the momentum equation across the wall jet velocity profile. The integral form of the non-dimensional wall jet momentum equation derived by Coles [38] is given below:

$$\rho u_e^2\frac{d\theta}{dx} - (2\theta + \delta^*)\frac{dp}{dx} = \frac{\tau_w}{Re} \tag{4}$$

Where u_e is boundary layer edge velocity, δ^* is the displacement thickness, θ is the momentum thickness, and τ_w is the wall shear stress. If $\tau_w > 0$, the flow is attached. If $\tau_w < 0$, the flow is separated.

Eq. (4) can be further rewritten as:

$$(2\theta + \delta^*)(S - \frac{dp}{dx}) = \frac{\tau_w}{Re} \tag{5}$$

Where $S = Qd\theta/dx$ and $Q = \rho u_e^2/(2\theta + \delta^*)$. Q represents the convection terms expressed by the dynamic pressure augmented by the wall jet momentum and displacement thickness in the denominator.

In APG, terms δ^* and θ are usually positive. If $S > dp/dx$, then $\tau_w > 0$, the flow is attached. If $S < dp/dx$, then $\tau_w < 0$, the flow is separated. This provides a quantitative criterion to evaluate flow separation.

Eq. (5) can be used to analyze the separation control mechanism in the same way as the differential equation (1). The enhancement of both the spanwise vorticity ω_z magnitude and streamwise mass flow will increase Q factor and S factor by reducing θ and δ^*. For a wall jet in

an adverse pressure gradient, $d\theta/dx$ is always positive due to boundary layer momentum loss. Therefore, the S factor is always positive to offset APG, dp/dx in Eq. (5). The quantification in later Sections is to see how CFWJ can enhance the S factor to achieve $\tau_w > 0$.

3. Numerical approaches

With the analysis framework established in Section 2, the following sections aim to analyze the CFWJ separation control mechanism based on the framework and support the analysis by quantitative results. This section addresses the setups of the current numerical study, including numerical methods, model geometry, meshes, boundary conditions, and validations.

3.1. Governing equations

The governing equations for the CFD simulation are the unsteady Reynolds averaged Navier-Stokes equations (URANS) with one equation Spalart-Allmaras turbulence model [39], which are solved in a fully coupled manner using an implicit unfactored Gauss-Seidel line iteration to achieve high convergence rate. The normalized Navier-Stokes governing equations in generalized coordinates are given by:

$$\frac{\partial \mathbf{Q}}{\partial t} + \frac{\partial \mathbf{E}}{\partial \xi} + \frac{\partial \mathbf{F}}{\partial \eta} + \frac{\partial \mathbf{G}}{\partial \zeta} = \frac{1}{Re}\left[\frac{\partial \mathbf{R}}{\partial \xi} + \frac{\partial \mathbf{S}}{\partial \eta} + \frac{\partial \mathbf{T}}{\partial \zeta}\right] + \mathbf{S}_v \tag{6}$$

where Re is the Reynolds number. As described for the normalization of Eq. (1), the Reynolds number in Eq. (6) is not intended to be the scaling Reynolds number for the co-flow wall jet. The Reynolds number in this study is determined by the NASA hump chord length and the inlet flow conditions, which is the same as that used in the experimental study of Seifert and Pack [40]. Their research indicates that the flow control effectiveness is not sensitive to the way of the Reynolds number determined, i.e., by the chord length, slot height, or upstream boundary layer momentum thickness. The conservative variable vector $\mathbf{Q}$, inviscid flux $\mathbf{E}$, viscous flux vector $\mathbf{R}$ are expressed as follows, and the rest can be expressed following the symmetric rule.

$$\mathbf{Q} = \frac{1}{J}\begin{bmatrix} \rho \\ \rho u \\ \rho v \\ \rho w \\ \rho e \\ \rho \hat{\nu} \end{bmatrix}, \mathbf{E} = \frac{1}{J}\begin{bmatrix} \rho U \\ \rho u U + p\xi_x \\ \rho v U + p\xi_y \\ \rho w U + p\xi_z \\ (\rho e + p)U \\ \rho \hat{\nu} U \end{bmatrix},$$

$$\mathbf{R} = \frac{1}{J}\begin{bmatrix} 0 \\ \tau_{xi}\xi_i \\ \tau_{yi}\xi_i \\ \tau_{zi}\xi_i \\ (u_j\tau_{ij} - q_i)\xi_i \\ \frac{\rho}{\sigma}(\nu + \hat{\nu})\frac{\partial \hat{\nu}}{\partial x_i}\xi_i \end{bmatrix}, \mathbf{S}_v = \begin{bmatrix} 0 \\ 0 \\ 0 \\ 0 \\ 0 \\ S_\nu \end{bmatrix}$$

The $\mathbf{S}_v$ in Eq. (6) is the source term for the S-A model,

$$\begin{aligned} S_\nu = \frac{1}{J}\Bigg[& \frac{1}{Re}\left[-\rho\left(c_{w1}f_w - \frac{c_{b1}}{\kappa^2}f_{t2}\right)\left(\frac{\tilde{\nu}}{d}\right)^2\right] \\ & + \frac{1}{Re}\left[\frac{\rho}{\sigma}c_{b2}(\nabla\tilde{\nu})^2 - \frac{1}{\sigma}(\nu + \tilde{\nu})\nabla\tilde{\nu}\bullet\nabla\rho\right] \\ & + Re\left[\rho f_{t1}(\Delta q)^2\right] + \rho c_{b1}\left(1 - f_{t2}\right)\tilde{S}\tilde{\nu}\Bigg] \end{aligned} \tag{7}$$

Other auxiliary relations and coefficients for the S-A turbulence model can be found in [39,41].

3.2. Navier-Stokes equations solver

The in-house high order CFD code Flow-Acoustics-Structure Interaction Package (FASIP) is used to solve the 2D unsteady-Reynolds averaged Navier-Stokes equations with one equation Spalart-Allmaras (S-A) turbulence model [39]. A 3rd order WENO scheme for the inviscid flux [42,43] and a 4th order central differencing for the viscous terms [43] are employed to discretize the Navier-Stokes equations. The low diffusion E-CUSP scheme suggested by Zha et al. [44] based on the Zha-Bilgen flux vector splitting [42] is utilized with the WENO scheme to evaluate the inviscid fluxes. All the simulations in this study are conducted as unsteady time accurate simulations. The second order time-accurate implicit time marching method with pseudo time and Gauss-Seidel line relaxation is used to achieve a fast convergence rate [45,46]. The FASIP code is intensively validated for CFWJ simulations [8,30,47–49]. The time-averaged results are presented after the flows and all the aerodynamic forces become dynamically stable.

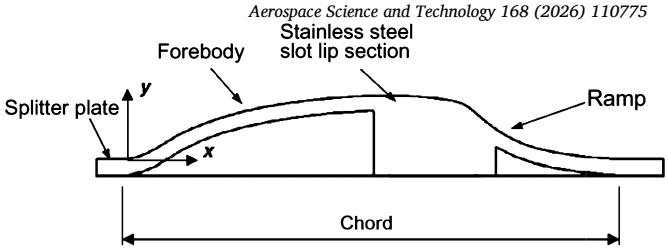

Fig. 2. Geometry of the hump upper surface [50].

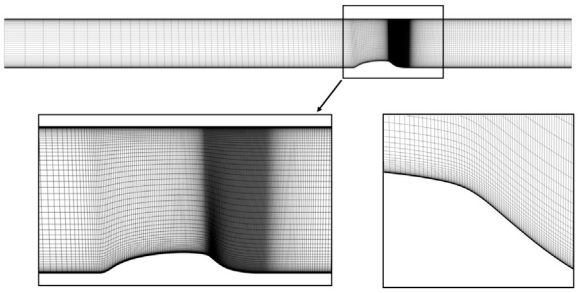

Fig. 3. 2D computational mesh of baseline hump with zoomed view on the surface mesh.

Table 1
Details of the mesh sizes.

Meshes	Hump	Injection duct	Suction plenum
Baseline	408×108	40×80	62×112
Refined	816×216	80×160	124×224

3.3. Mesh and boundary conditions

The baseline NASA hump configuration with no flow control is designed to have a converging section followed by a rapid area expansion downstream of the throat as shown in Fig. 2, which creates a severe diffusion and massive flow separation.

As shown in Fig. 3, the computational domain with a mesh of 408×108 = 44,064 cells is created based on the experimental setups described in references [50,51]. Details of mesh sizes are shown in Table 1.

The boundary conditions (BCs) set-up is illustrated in Fig. 4. The inlet is located at 6C upstream of the hump and the outlet is at 3C downstream of the hump. The total pressure, total temperature, and flow angle are specified at the inlet as the boundary conditions. Static pressure is specified at the outlet boundary. The top wall is 0.9 C away from the bottom as designed in the experiments [50,51]. No-slip wall BC is enforced on all the walls. Note that the original NASA case modified the top surface with a slight downward step, and with the slip wall boundary condition, the blockage effect can be reproduced. Different from such a treatment, we applied the no-slip wall boundary condition on the unmodified top surface to directly model the blockage effect.

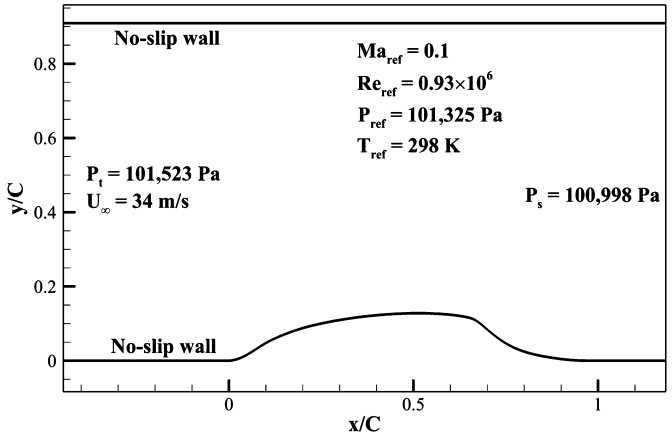

Fig. 4. Boundary conditions of baseline hump simulation and the reference conditions.

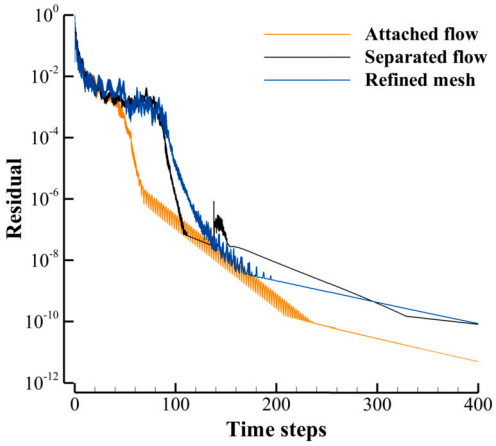

Fig. 5. Convergence history of typical cases.

The unsteady simulation uses a constant non-dimensional characteristic time step $\Delta\tilde{t} = 5\times10^{-3}$ with the maximum L_2-norm residual typically reduced by 2 orders of magnitude within less than 40 pseudo time iterations per physical time step. Fig. 5 shows three typical convergence histories with time for three unsteady simulations, including a separated baseline flow and its associated mesh refinement result, and an attached flow with flow control. The L2-Norm residual of the unsteady Navier-Stokes equations is basically driven to machine zero with 400 characteristic time, indicating the full convergence of the unsteady Navier-Stokes equations. All the cases in the present numerical study achieve a similar convergence, which ensures the reliability of the results.

3.4. Validations of numerical simulation

The experimental baseline hump, steady injection, and suction cases [51,52] are used to validate the simulation. All the location positions are measured from the hump leading-edge referring to Fig. 4.

3.4.1. Validation of baseline NASA hump

The NASA hump is widely used as a benchmark case to validate numerical algorithms and turbulence modeling [52]. Previous studies have tested various turbulence models, demonstrating that the S-A model produced no significant differences compared to other models such as SST and SSG/LRR-RSM in terms of pressure coefficient distribution, skin friction coefficient (particularly in the region $0 < x/C < 1$), separation onset, and reattachment location [52]. Furthermore, this paper aims to study the mechanism of how CFWJ attaches flow in the adverse pressure gradient. The S-A model is widely recognized to represent turbulent characteristics well for attached turbulent boundary layers. Therefore, the S-A model is suitable for the purpose of this study.

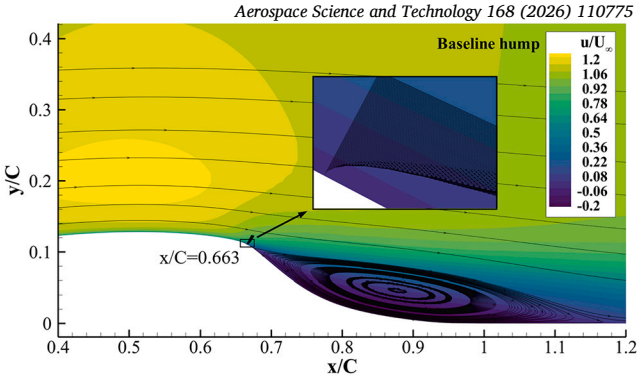

Fig. 6. Normalized x-directional velocity (u/U_∞) contours of the baseline hump with the separation onset location and velocity profile.

To validate the FASIP code, the current CFD simulations use the same experimental Mach number and Reynolds number. In experiments, the hump model was tested in an open-return wind tunnel with freestream velocity of $U_\infty = 34$ m/s (Mach = 0.1). The Reynolds number for all the cases is 0.93×10^6 based on the hump chord length. Mesh refinement studies are also conducted by doubling the number of grid points in i, j direction simultaneously. The sizes of the baseline and refined meshes are given in Table 1.

Fig. 6 shows the normalized x-directional velocity (u/U_∞) contours of the baseline hump with the zoomed view of the velocity profile at the separation onset location. Fig. 7 compares the skin friction coefficient C_f and the pressure coefficient C_p with experimental data. The numerically-computed C_f in Fig. 7 (a) indicates that the flow separation onset occurs at $x/C = 0.663$ ($\tau_w = 0$) and reattaches at $x/C = 1.17$, which agree well with the experimental measurement with separation inception point at 0.665 and reattachment at 1.11 ± 0.003 [50,53]. Downstream of the reattachment point beyond $x/C = 1$ in Fig. 7 (a), the deviation between the numerical and experimental C_f is due to the inadequacy of the S-A turbulence model to resolve the severe flow separation. A similar discrepancy is reported by Rumsey [52] and Naughton et al. [54].

Fig. 7 (b) is the numerically-computed C_p distributions (in black) of the baseline hump compared with the experiment [50,51]. Following the practice by Rumsey [52] and Kara et al. [55], the numerically-computed time-averaged C_p distributions are shifted by -0.033 to match the experimental upstream reference conditions. As shown in Fig. 7 (b), the simulated C_p distributions of the baseline hump agree very well with experimental measurement, except that the pressure drop at $0.6 < x/C < 0.9$ is slightly underestimated. A similar discrepancy is also reported by other researchers [52,55].

3.4.2. Validation of the hump with injection

To further validate the numerical simulation of jet injection, the hump case with steady injection only is simulated and compared with the experiment. The blowing actuator is located at $x/C = 0.68$ and is angled at 10° to the bottom wall as described in Ref. [51]. Fig. 8 (a) is the velocity contours of steady injection only case with $U_j = 85$ m/s ($C_\mu = 0.9\%$) used in the experiment [51]. The boundary conditions and case set-up are the same as those used by Borgmann et al. [51] and Tang et al. [56]. The steady-blowing jet fully attaches the flow. The C_p distributions in Fig. 8 (b) shows that the numerically-computed pressure distribution is again in very good agreement with the experiment [51]. The spike downstream of the low-pressure suction peak is due to the jet injection. The solution is converged based on the mesh refinement as shown in Fig. 8 (b).

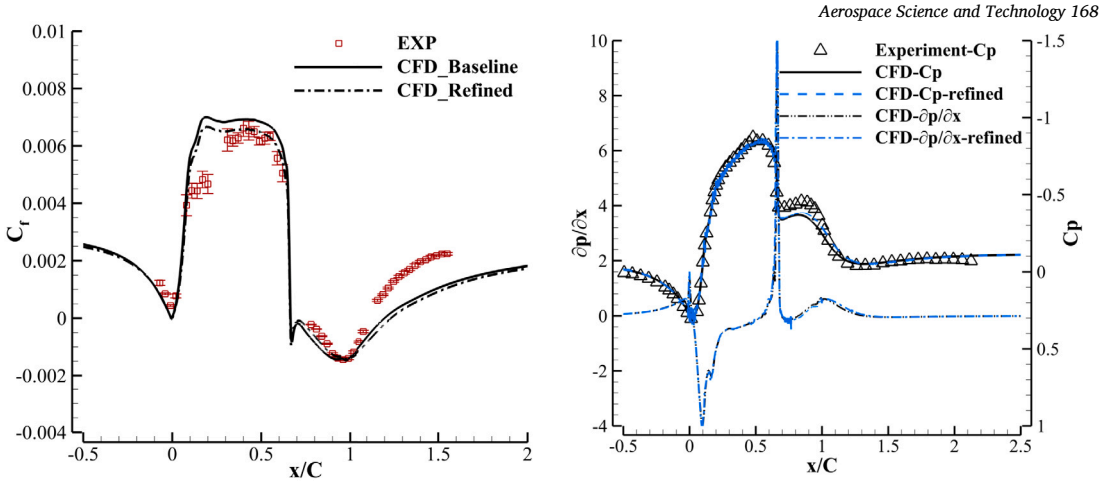

(a) Skin friction coefficient C_f (b) Pressure coefficient C_p

Fig. 7. Comparison of the C_f and C_p distribution with experimental data. $\partial p/\partial x$ is the plot of streamwise pressure gradient.

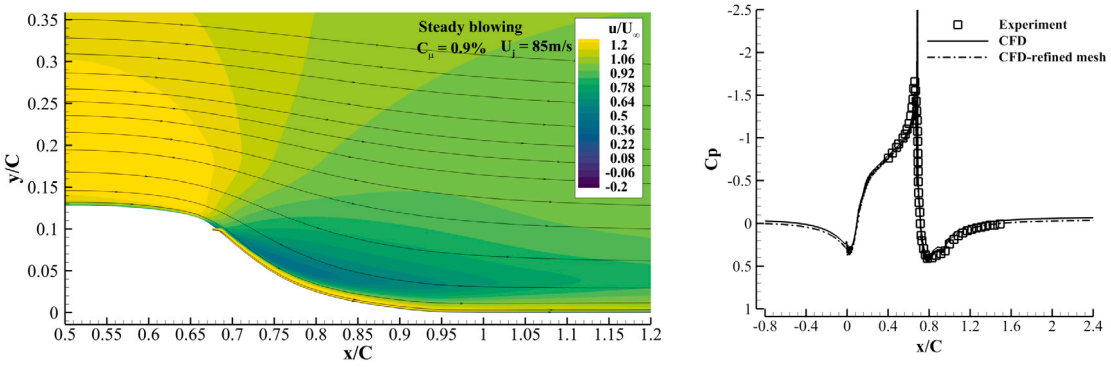

(a) Normalized x-directional velocity (u/U_∞) contours (b) C_p distributions

Fig. 8. CFD results of the hump with steady blowing.

3.4.3. Validation of the hump with suction

The last validation case is the one using steady suction only with C_μ of 0.241% (mass flow coefficient $C_Q =$ 0.15% [57]). For the suction-only case, the hump geometry is the same as the baseline case with a suction plenum located at $x/C = 0.65$ and the mesh is directly adopted from the NASA source [52]. The computed velocity contour in Fig. 9 indicates that the suction-only flow control at the current C_μ is not adequate to remove the flow separation, which is consistent with the experimental observation. The numerically-computed C_p distributions with mesh refinement are shown in Fig. 9. The CFD results are in good agreement with the experiment [52], but with the pressure rise under-predicted at $0.6 < x/C < 1.2$, which indicates that the separation bubble thickness may be over-predicted. A similar discrepancy is observed in the URANS simulations conducted by other researchers [58,59]. Further increase of the mesh size does not change the results as shown by the mesh refinement in Fig. 9 (b).

4. Separation control mechanism of CFWJ

In the CFWJ simulation as shown in Fig. 10, the micro-compressor actuator is simulated by applying total pressure inlet BC at the injection slot and static pressure outlet BC at the suction slot. An iteration is conducted to match the suction mass flow rate to the injection one within a tolerance of 1%. This treatment of the injection and suction is thoroughly validated in the previous work [8,9,30,60–62].

In our prior work [7], we examined a total of 13 cases to investigate the individual effects of CFWJ injection and suction. These cases are categorized by applying the injection in different pressure gradients. The injection is applied in the adverse pressure gradient region for Cases 1-7 and in the favorable pressure gradient region for Cases 8-13. Here, we present the most efficient configuration from each category. All the flows are attached with minimum energy consumption. The two cases are CFWJ Case 2 and Case 9, as shown in Fig. 11. Specifically, Case 2 has the injection at 67.5%C, and Case 9 has the suction at 70%C. These two cases represent the CFWJ with injection dominant and suction dominant cases respectively by placing the injection or suction close to the baseline separation onset point at 66.3%, but both are slightly downstream of the separation onset point in the region of adverse pressure gradient [7]. The momentum coefficient C_μ is defined in Eq. (8), where $\dot{m}$ is the CFWJ mass flow rate, U_j is the injection velocity, and A_{ref} is the reference area (hump platform area). The C_μ used is 0.85% for Case 2 and 0.77% for Case 9, which are the minimum C_μ to achieve full flow attachment for these two cases respectively [7].

$$C_\mu = \frac{\dot{m} U_j}{\frac{1}{2}\rho_{ref} {U_\infty}^2 A_{ref}} \tag{8}$$

The CFWJ power required is defined by the total enthalpy rise from the suction duct outlet (compressor inlet) to the injection duct inlet (compressor outlet) [63]. The expression for power required (PR) and the non-dimensional power coefficient (P_c) are defined as follows, where, H_{t2} is the total enthalpy at the suction slot, Γ is the total pressure ratio between the injection and suction, and γ is the specific heat ratio with a value of 1.4 for ideal gas. The minimum P_c required for Case 2 to achieve full flow attachment is 0.003, which is lower than that of Case

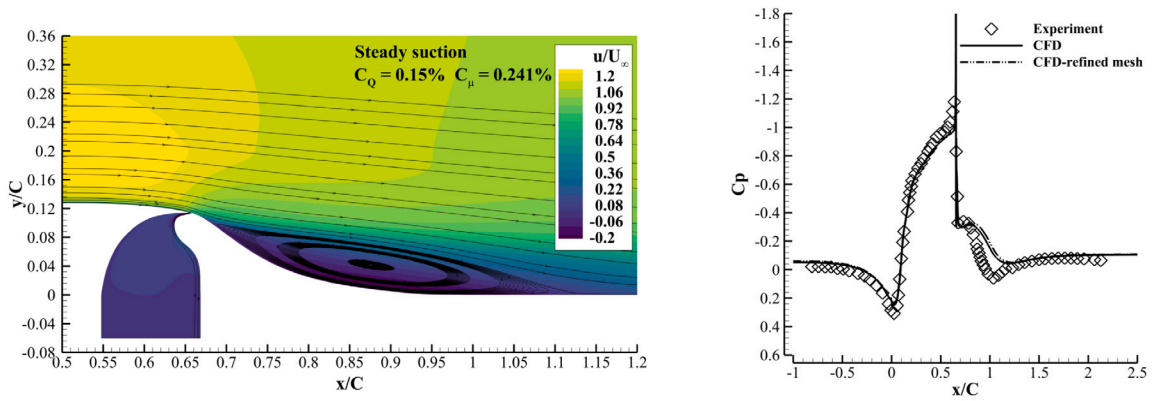

(a) Normalized x-directional velocity (u/U_∞) contours (b) C_p distributions

Fig. 9. CFD results of the hump with steady suction.

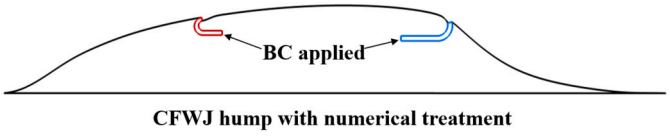

Fig. 10. Numerical treatment of the CFWJ hump. Injection and suction ducts are colored by red and blue, respectively. Micro-compressor is numerically treated by boundary conditions. (For interpretation of the colors in the figure(s), the reader is referred to the web version of this article.)

9 of 0.0032. Increasing C_μ in Case 9 to the same value as Case 2 will further increase P_c, leading to an excessive energy consumption.

$$PR = \dot{m} H_{t2} (\Gamma^{\frac{\gamma-1}{\gamma}} - 1) \tag{9}$$

$$P_c = \frac{PR}{\frac{1}{2}\rho_{ref} U_{ref}^3 A_{ref}} \tag{10}$$

4.1. Injection placed near separation onset point

Fig. 12 shows the spanwise vorticity contours and velocity profiles at five streamwise stations along the co-flow wall jet for CFWJ Case 2, which has the entire CFWJ immersed in adverse pressure gradient region. The velocity profile at Station 1 upstream of the injection slot is a typical wall boundary layer profile, which is energized by the downstream CFWJ and would be nearly separated otherwise. The velocity profile at Station 2 downstream of the injection slot has a protruding profile close to the wall, a typical wall jet profile. In the adverse pressure gradient, the wall jet profile becomes more smeared flowing downstream due to mixing with the mainstream as shown at Stations 3 and 4. Further beyond the suction slot, the velocity profile returns to a typical boundary layer profile but is energized as shown in Station 5.

There are three counter-rotating layers of vorticity observed clearly downstream of the injection slot in Fig. 12, a layer of clockwise vorticity due to the wall jet boundary layer in blue, a layer of counter-clockwise vorticity due to the wall jet in red, a zero vorticity layer between the two counter-rotating vorticity layers in white, and a layer of clockwise vorticity due to the main flow boundary layer mixing with the wall jet in blue. With the CFWJ flowing downstream, the wall jet counter-clockwise vorticity layer is decayed and dissipated due to mixing and disappears downstream of the suction slot when the CFWJ ends.

The pressure coefficient distribution along the wall in Fig. 13 indicates that CFWJ Cases 2 and 9 have the peak velocity much more augmented compared with the baseline due to the removal of flow separation. The pressure spikes at the x/C, about 0.5 and 0.9 are caused by the injection and suction slots due to slot opening and sharp lip acceleration. More details are discussed in Ref. [7].

The boundary layer profiles of CFWJ Case 2 with the injection at 67.5%C are analyzed based on the wall jet differential Eq. (1) and (3) and integral Eq. (5) to investigate the injection effects. Fig. 14 (a) shows the transverse distributions of the terms in Eq. (3) normal to the wall surface at the location 2%C downstream of the injection slot. The extraction location is chosen to be close enough to the injection (or suction) slot to best capture the jet effects, while also avoiding regions near the slot-hump transition surfaces, which could otherwise introduce artificial errors. The distances of 2%C downstream of the injection slot and 1.5%C upstream of the suction slot (in Section 4.2) are also determined in a trade study that are effective at the closest position to the slots. The profiles are plotted in Fig. 14 against the normal distance from the wall normalized by the injection slot height (D/h). For better demonstration, R is the summation of the first three terms of Eq. (1), which is the resultant factor to offset the adverse pressure gradient. LHS_D is the summation of all the terms on the left-hand side of Eq. (1).

The flow is attached by CFWJ at this location as shown in Fig. 14, but has $[\partial^2 u/\partial y^2]_{D/h=0} > 0$ ($LHS_D > 0$, Eq. (1)) at the wall. This is because the summation of the first three terms, R in Eq. (1), is basically zero at the wall due to the no-slip zero velocity with constant molecular viscosity. Eq. (1) returns to the compatibility condition [64, p. 133] at the wall as expressed by Eq. (11). The $[\partial^2 u/\partial y^2]_{D/h=0}$ solely depends on the local pressure gradient with positive sign in APG no matter the flow is separated or attached. A flow in APG can be very well attached with $[\partial^2 u/\partial y^2]_{D/h=0} > 0$ as shown here.

$$\left.\frac{\partial p}{\partial x}\right|_{y=0} = \mu \left.\frac{\partial^2 u}{\partial y^2}\right|_{y=0} \approx -\mu \left.\frac{\partial \omega_z}{\partial y}\right|_{y=0} \tag{11}$$

The compatibility condition Eq. (11) indicates that an increasing spanwise clockwise vorticity distribution normal to the wall is a necessary condition to attach flow in adverse pressure gradient. The greater the adverse pressure gradient, the higher the gradient of vorticity magnitude needs to be. A strong wall jet injection with the protruding profile provides a high $\partial\omega_z/\partial y$ at the wall to satisfy the compatibility condition. Such a vorticity gradient is provided by a wall-jet-enhanced turbulent boundary layer due to the rapid velocity increasing rate beyond the thin linear viscous sub-layer, as shown by Fig. 14 (b). The stream-wise suction also has the similar effect.

Away from the wall as shown in Fig. 14 (a), the adverse pressure gradient is offset by the rapidly increasing magnitude of R with a negative sign. Among the first three terms in Eq. (3), the turbulent diffusion $\omega_z \partial\mu/\partial y/Re$ makes the largest contribution to offset the adverse pressure gradient. This is attributed to the large gradient of the eddy viscosity ($\partial\mu_t/\partial y$) and large spanwise vorticity (ω_z) of the wall jet as shown

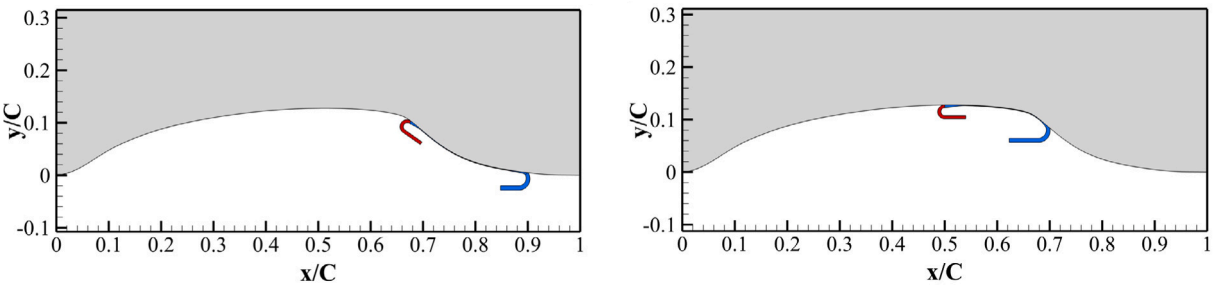

Fig. 11. Configurations of the CFWJ NASA hump. The dominant location means near separation onset.

Table 2
CFWJ Case 2, terms in Eq. (3) at $y^+ = 2$ at 2%C downstream of the injection slot.

Cases	Location	C_μ	$\rho u \partial u/\partial x$	$-\rho v \omega_z$	$\omega_z \partial \mu/\partial y/Re$	$\partial p/\partial x$	LHS_D
CFWJ 2	69.5%C	0.85%	-5.15	1.77	-18.54	10.33	-11.59

Table 3
CFWJ Case 2, terms in Eq. (5) at 2%C downstream of the injection slot.

Cases	Location	C_μ	δ^*	θ	$d\theta/dx$	$\mathcal{Q}$	S	dp/dx	LHS_I
CFWJ 2	69.5%C	0.85%	5.70×10^{-3}	3.97×10^{-3}	0.17	69.38	11.52	3.34	1.12×10^{-1}

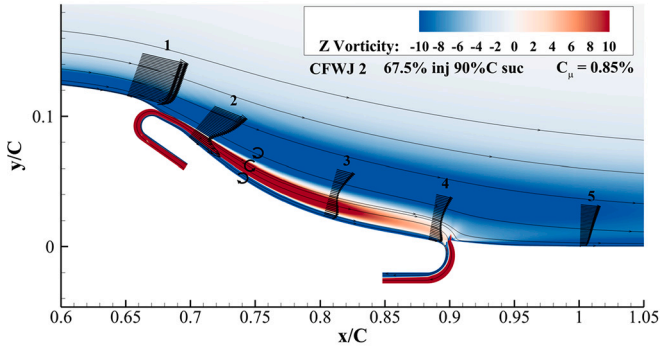

Fig. 12. Spanwise vorticity contours showing three vorticity layers. Velocity profiles at five stations of the CFWJ Case 2.

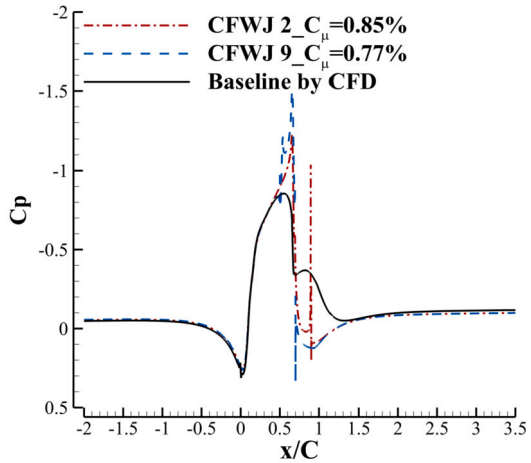

Fig. 13. C_p distribution of the baseline case, Case 2, and Case 9.

in Fig. 14 (b), which transfers the momentum transversely to energize the boundary layer. Such an effect may be insignificant for an adiabatic incompressible laminar wall jet since the viscosity gradient would be near zero.

Also shown in Fig. 14 (a), the second-largest contribution to offset adverse pressure gradient is the streamwise inertia term $\rho u \partial u/\partial x$ exerted by the effects of CFWJ injection that boosts ρu. An adverse pressure gradient makes $\partial u/\partial x$ negative and thus the whole term is against the adverse pressure gradient. The larger the APG, the greater magnitude of the $\partial u/\partial x$. Thus the capability of the streamwise inertia term to offset the APG will grow with the increasing APG, as long as the velocity profile is established to match the compatibility condition. The transverse convective term ($-\rho v \omega_z$ or $\rho v \partial u/\partial y$) has a smaller positive value contributing to the opposite for flow attachment. The reason can be explained below based on the continuity equation:

$$\frac{\partial v}{\partial y} = -\frac{\partial u}{\partial x} \tag{12}$$

The right hand side of Eq. (12) is positive due to a decreasing u in APG, which makes the v increase in the transverse direction (y). Since velocity is zero on the wall, v has to be positive above the wall. This leads to the positive convective term ($\rho v \partial u/\partial y$ or $-\rho v \omega_z$) that penalize the wall jet effect of separation mitigation. The larger the positive value, the greater the penalty. Even though $v << u$, the transverse convective term ($\rho v \partial u/\partial y$ or $-\rho v \omega_z$) can be at a similar order of magnitude to the $\rho u \partial u/\partial x$ term because the velocity gradient $\partial u/\partial y$, or the vorticity ω_z is large due to the wall jet, as shown in Fig. 14 (b).

This also suggests that a tangential injection is desirable since it has the minimum v and thus a minimal effect to enhance the adverse pressure gradient. If the jet injection has an angle extruding to the main flow, there will be a large positive v that enhances the flow separation. For example, a strong jet injection 90° normal to the main flow would create a large flow blockage and separation.

The relations among the terms of the wall jet momentum Eq. (3) described above are clearly seen in Table 2 with the quantitative values of Case 2 at $y^+ = 2$. The LHS_D already becomes negative at this location.

Table 3 presents the quantitative values of each term in wall jet integral Eq. (5), where LHS_I is the summation of all the terms on the left-hand side. A CFWJ enhances the clockwise vorticity near the wall and reduces θ and δ^*, which increases the $\mathcal{Q}$ factor. As a result, the S factor is much larger than dp/dx and therefore keeps LHS_I value pos-

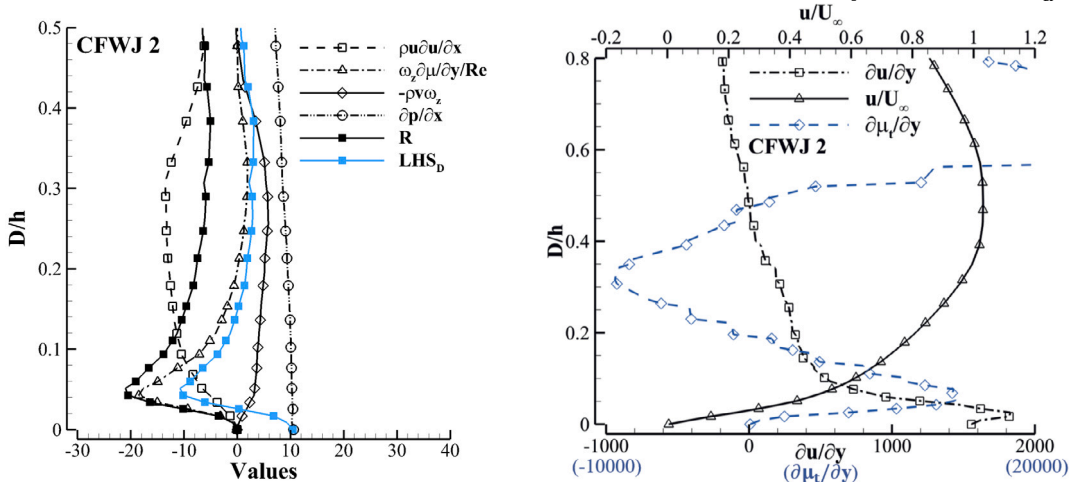

(a) Terms in Eq. (3) (b) Profiles of velocity, $\partial u/\partial y$, and $\partial \mu_t/\partial y$

Fig. 14. Distributions of different terms in Eq. (3) at 2%C downstream of the injection slot with $C_\mu = 0.85\%$.

Table 4
CFWJ Case 9, terms in Eq. (3) at $y^+ = 2$ at 1.5%C upstream of the suction slot.

Cases	Location	C_μ	$\rho u \partial u/\partial x$	$\rho v \partial u/\partial y$	$-\partial u/\partial y \partial \mu/\partial y/Re$	$\partial p/\partial x$	LHS_D
CFWJ 9	68.5%C	0.77%	-1.53	-8.91	-18.16	8.31	-20.29

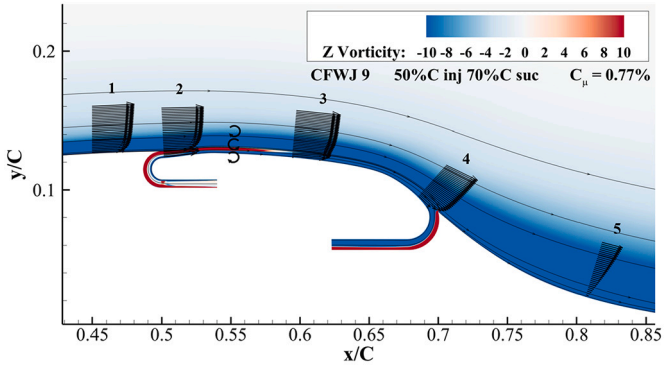

Fig. 15. Spanwise vorticity contours showing three vorticity layers near injection slot. Velocity profiles at five stations of the CFWJ Case 9.

itive, indicating an attached flow with $\tau_w > 0$. The results in Table 3 are aligned with the analysis based on the turbulent wall jet differential equation of Table 2.

4.2. Suction placed near separation onset point

Fig. 15 shows the vorticity contours of CFWJ Case 9 with velocity profiles at five locations. The injection of CFWJ Case 9 is located upstream in the region of a favorable pressure gradient. In the CFWJ injection region, Fig. 15 indicates a wall jet velocity profile and 3 layers of counter-rotating vortex layers, which are thinner and shorter than those in Case 2 in adverse pressure gradient.

Fig. 16 compares the velocity profiles of Cases 2 and 9 at three common locations. At the location $x/C = 0.6$ in Fig. 16 (a), Case 2 has a typical turbulent boundary layer profile and Case 9 has slightly protruding velocity profile due to the upstream wall jet injection. In Fig. 16 (b), $x/C = 0.7$ locates downstream the injection slot of Case 2 whose velocity profile presents a pronounced protruding pattern due to the wall jet injection. For Case 9, $x/C = 0.7$ is immediately downstream of the suction slot, however, its velocity profile is significantly weaker than that of Case 2. In further downstream at $x/C = 0.8$ as shown in Fig. 16 (c), the pronounced wall jet profile becomes smeared in Case 2 but still with strong near wall momentum. Comparatively, Case 9 has velocity profile further weakened due to overcoming the adverse pressure gradient at the geometric diverging region.

Fig. 17 is the profiles of the different terms of the wall jet momentum Eq. (1) for CFWJ Case 9 to show the suction dominant effect of CFWJ. The profiles are plotted at 68.5%C location, 1.5%C upstream of the suction slots. Again, LHS_D begins with a positive value at the wall due to the effect of adverse pressure gradient. Away from the wall, the LHS_D rapidly returns negative to match the attached flow concave velocity profile. The quantitative contributions near the wall with $y^+ = 2$ are listed in Table 4. The dominant term off-setting adverse pressure gradient for this case is again the turbulent diffusion term $-\partial u/\partial y \cdot \partial \mu/\partial y/Re$ as shown in Fig. 17 and Table 4. This is attributed to the streamwise suction that creates an acceleration within the boundary layer with increased wall spanwise vorticity. The transverse convection term $\rho v \partial u/\partial y$, or the wall vorticity flux, has a much larger contribution to offset the APG than the injection dominant Case 2. This is benefited from the negative vertical velocity component pointing to the wall due to the suction and the high spanwise vorticity that the suction induces. That is, for the CFWJ suction, all the first three terms in Eq. (1) contribute significantly to offset the adverse pressure gradient. This streamwise suction capability to offset the APG also grows with the APG.

Table 5 compares the values of each term of the integral form momentum Eq. (5) for CFWJ Case 9. The measured location is the same as that for the differential momentum equation in Table 4 at 1.5%C upstream of the suction slot. The streamwise suction combined with the more-upstream injection substantially thins the boundary layer than Case 2 with δ^* and θ reduced by more than 50%. With the reduced δ^* and θ, the compound S factor in Eq. (5) is substantially increased to offset the adverse pressure gradient and attach the flow. Overall, both CFWJ cases have sufficient S factor to offset the adverse pressure gradient and make the sign of LHS_I, i.e., the wall shear stress, positive with the attached elevated flow.

The analysis in this section indicates that both CFWJ injection and suction contribute to overcoming adverse pressure gradients and sup-

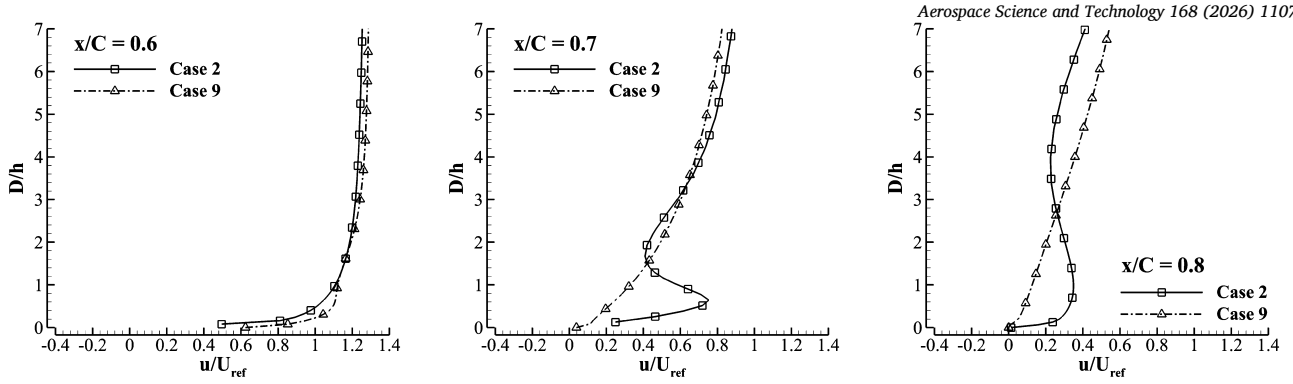

(a) x/C=0.6 (b) x/C=0.7 (c) x/C=0.8

Fig. 16. Velocity profiles comparison for Case 2 and Case 9 at three locations.

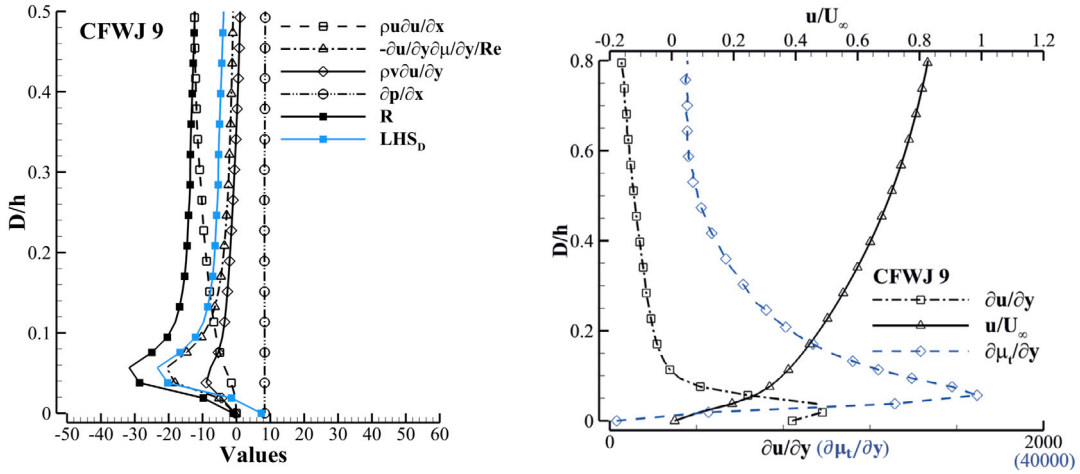

(a) Terms in Eq. (3) (b) Profiles of velocity, $\partial u/\partial y$, and $\partial \mu_t/\partial y$

Fig. 17. Distributions of different terms in Eq. (3) at 1.5%C upstream of the suction slot.

Table 5
CFWJ Case 9, terms in Eq. (5) at 1.5%C upstream of the suction slot.

Cases	Location	C_μ	δ^*	θ	$d\theta/dx$	Q	S	dp/dx	LHS_I
CFWJ 9	68.5%C	0.77%	2.02×10^{-3}	1.21×10^{-3}	0.12	211.33	25.30	7.22	8.03×10^{-2}

pressing flow separation. The necessary condition to attach the flow in APG is that a velocity profile with a positive $\partial u/\partial y$ (spanwise clockwise vorticity $\omega_z < 0$) and a positive gradient of the vorticity magnitude are established by injection, or suction, or their combined effects. To effectively and efficiently achieve such a velocity profile and vorticity distribution, either the injection or suction needs to be placed near the flow separation onset location where the flow has the largest adverse pressure gradient, but is not largely separated yet. Otherwise, placing both the injection and suction in a deep separation region simultaneously will neither be efficient nor effective in establishing the required velocity profile.

It should be noted that the present study adopts a two-dimensional framework to isolate and understand the fundamental separation control mechanism of CFWJ. The real-world flows are inherently three-dimensional. Spanwise momentum transfer and crossflow instabilities can redistribute vorticity and turbulent diffusion, potentially changing the local effects on the adverse pressure gradient. Nevertheless, the mechanism study of CFWJ is more qualitative than quantitative, and in the time average sense, the 3D boundary layer flow structure may not be very significant for the study.

5. Conclusions

Based on the validated 2D URANS numerical simulation of the NASA hump with CFWJ flow control and the analysis of wall jet momentum equations, the following conclusions are drawn:

1. The CFWJ working mechanism includes the following three factors. 1) CFWJ establishes sufficient clockwise spanwise vorticity and positive transverse gradient of vorticity magnitude at the wall by tangential injection and streamwise suction. This is essential to offset the APG by enhancing the turbulent diffusion and the wall vorticity flux. 2) The wall jet provides the required streamwise mass flux to enhance the streamwise inertia force that offsets the APG. 3) The control effects of turbulent diffusion and the streamwise inertia force grow with APG provided that the factor 1) and 2) are sufficiently established.
2. Turbulent diffusion near the wall is the most dominant term to offset adverse pressure gradient for both the CFWJ injection and suction. It plays a key role in wall jet mixing and energizing the wall boundary layer.

3. The CFWJ injection has a typical wall jet velocity profile with three counter-rotating vorticity layers. The suction does not create the counter-rotating vorticity layers. For a CFWJ injection, keeping the injection tangential to the wall surface is most effective to minimize flow blockage, maximize the spanwise vorticity, turbulent diffusion, and streamwise inertia force to offset the adverse pressure gradient. For a CFWJ suction, a streamwise suction not only enhances those same terms enhanced by the injection, but also augments the transverse momentum term due to the velocity component pointing to the wall.

CRediT authorship contribution statement

Kewei Xu: Writing – review & editing, Writing – original draft, Visualization, Validation, Methodology, Investigation, Funding acquisition, Formal analysis, Data curation, Conceptualization. **Yan Ren:** Validation, Investigation. **Gecheng Zha:** Writing – review & editing, Validation, Supervision, Software, Resources, Project administration, Methodology, Investigation.

Declaration of competing interest

The authors declare the following financial interests/personal relationships which may be considered as potential competing interests: Disclosure: The University of Miami and Dr. Gecheng Zha may receive royalties for future commercialization of the intellectual property used in this study. The University of Miami is also an equity owner in CoFlow Jet, LLC, license of the intellectual property used in this study. If there are other authors, they declare that they have no known competing financial interests or personal relationships that could have appeared to influence the work reported in this paper.

Acknowledgement

We would also like to thank Dr. Meng Wang at the University of Notre Dame for his very helpful discussion. The authors would like to acknowledge the computing resource provided by the Center of Computational Sciences at the University of Miami. The lead author would also like to acknowledge the start-up funding provided by the Office of the Vice President for Research and Dean of the Graduate School at the University of Maine.

Data availability

Data will be made available on request.

References

[1] M. Gad-el-Hak, Flow Control, Passive, Active, and Reactive Flow Management, Cambridge University Press, 2000.
[2] L. Prandtl, Über Flüssigkeitsbewegung bei sehr kleiner Reibugn, in: Proc. Third Int. Math. Cong., Heidelberg, Germany, 1904, pp. 484–491.
[3] W. Xie, Z. Luo, Y. Zhou, P. Cheng, Q. Liu, W. Peng, X. Deng, Influence of volume and frequency parameters on opposing plasma synthetic jet for drag reduction in supersonic flow, Aerosp. Sci. Technol. 146 (2024) 108971.
[4] Z. Trávníček, J. Kordík, Energetic efficiencies of synthetic jet actuators: commentary on the article by Gil and Strzelczyk, Exp. Therm. Fluid Sci. 98 (2018) 121–123.
[5] K. Lee, S. Kikuchi, Flow control by dielectric barrier discharge plasma actuators for a rectangular jet with inlet disturbance, Phys. Fluids 36 (3) (2024).
[6] H. Zong, Y. Wu, H. Liang, Z. Su, J. Li, Experimental study on q-learning control of airfoil trailing-edge flow separation using plasma synthetic jets, Phys. Fluids 36 (1) (2024).
[7] K. Xu, Y. Ren, G. Zha, Numerical analysis of energy expenditure for coflow wall jet separation control, AIAA J. 60 (5) (2022) 3267–3285.
[8] G.-C. Zha, C. Paxton, A. Conley, A. Wells, B. Carroll, Effect of injection slot size on high performance co-flow jet airfoil, AIAA J. Aircr. 43 (2006).
[9] K. Xu, G.-C. Zha, High control authority three-dimensional aircraft control surfaces using coflow jet, J. Aircr. 58 (1) (2021) 72–84.
[10] K. Xu, G. Zha, System energy benefit using co-flow jet active separation control for a serpentine duct, Aerosp. Sci. Technol. 128 (2022) 107746.
[11] K. Xu, G. Zha, Design of high specific speed mixed flow micro-compressor for co-flow jet actuators, in: Turbo Expo: Power for Land, Sea, and Air, vol. 58714, American Society of Mechanical Engineers, 2019, V008T26A014.
[12] B.E. Launder, W. Rodi, The turbulent wall jet - measurement and modeling, J. Fluid Mech. 15 (1983) 429–459, https://doi.org/10.1146/annurev.fl.15.010183.002241.
[13] R.J. Englar, Circulation control for high lift and drag generation on STOL aircraft, J. Aircr. 12 (1975) 457–463, https://doi.org/10.2514/3.59824.
[14] R.J. Englar, Circulation control pneumatic aerodynamics: Blown force and moment augmentation and modifications; past, present and future, AIAA Paper 2000-2541, 2000.
[15] G.S. Jones, Pneumatic flap performance for a 2D circulation control airfoil, stedy & pulsed, Chapter 7, in: R.D. Joslin, G.S. Jones (Eds.), Applications of circulation control technologies, in: Progress in Astronautics and Aeronautics, vol. 214, 2006, pp. 191–244.
[16] W.C. Sleeman Jr., W.C. Hohlweg, Low-Speed Wind Tunnel Investigation of a Four Engine Upper Surface Blown Model having a Swept Wing and Rectangular and D-Shaped Exhaust Nozzle, NASA TN D-8061, Dec. 1975.
[17] M. Sussman, J. Reed, USB Environment Assessment Based on YC-14 Flight Test Measurement, AIAA Paper 77-0593, Nov. 1981, https://doi.org/10.2514/6.1977-593.
[18] D.W. Riddle, R.C. Innis, J.L. Martin, J.A. Cochrane, Powered-Lift takeoff performance characteristics determined from flight test of the Quiet Short-Haul Research Aircraft /QSRA/, AIAA Paper 81-2409, in: AIAA Flight Testing Conference, Las Vegas, NV, Nov. 1981.
[19] J.K. Wimpress, C.F. Newberry, The YC-14 STOL Prototype: Its Design, Development and Flight Test, AIAA Case Study, AIAA, Reston, 1998.
[20] E. Forthmann, Turbulent Jet Expansion, NACA TM-789, March 1936.
[21] M.B. Glauert, The wall jet, J. Fluid Mech. (1956) 625–643, https://doi.org/10.1017/S002211205600041X.
[22] P. Bradshaw, M.T. Gee, Turbulent Wall Jets with and Without an External Stream, Aero. Res. Counc. R. & M., 1960, 3252.
[23] B. Newman, R. Patel, S. Savage, H. Tjio, Three-dimensional wall jet originating from a circular orifice, Aeronaut. Q. 23 (3) (1972) 188–200.
[24] I. Wygnanski, Y. Katz, E. Horev, On the applicability of various scaling laws to the turbulent wall jet, J. Fluid Mech. 234 (1992) 669–690.
[25] T. Dairay, V. Fortuné, E. Lamballais, L.-E. Brizzi, Direct numerical simulation of a turbulent jet impinging on a heated wall, J. Fluid Mech. 764 (2015) 362–394.
[26] T. Guo, M. Rau, P.P. Vlachos, S.V. Garimella, Axisymmetric wall jet development in confined jet impingement, Phys. Fluids 29 (2) (2017) 025102.
[27] A. Gupta, H. Choudhary, A. Singh, T. Prabhakaran, S. Dixit, Scaling mean velocity in two-dimensional turbulent wall jets, J. Fluid Mech. 891 (2020).
[28] B. McBreen, K. Xu, Y. Yang, Y. Ren, Y. Wang, G.-C. Zha, Numerical study of extreme adverse pressure gradients enabled by co-flow wall jet, in: AIAA Scitech 2023 Forum, 2023, p. 1430.
[29] A.M.O. Smith, High-Lift Aerodynamics, J. Aircr. 12 (1975) 501–530.
[30] Y. Yang, G. Zha, Super-lift coefficient of active flow control airfoil: what is the limit?, in: 55th AIAA Aerospace Sciences Meeting, 2017, p. 1693.
[31] G.-C. Zha, Y. Yang, Y. Ren, B. McBreen, Super-lift and thrusting airfoil of coflow jet actuated by micro-compressors, in: 2018 Flow Control Conference, 2018, p. 3061.
[32] S. Saranya, K. Balaji, M. Gor, S. Sulthan, Investigation into active and passive methods to enhance aerofoil aerodynamic performance, Int. J. Aeronaut. Space Sci. (2025) 1–11.
[33] B. Karuppiah, J.J. Wessley, Study on the influence of mass flow rate over a national advisory committee for aeronautics 6321 airfoil using improved blowing and suction system for effective boundary layer control, SAE Int. J. Aerosp. 14 (2021) 219–233 (01-14-02-0011).
[34] A. Katkar, K. Balajia, S. Khandal, Numerical studies on fixed wing aircraft aerodynamic performance using injection suction mechanism, Int. J. Veh. Struct. Syst. 14 (5) (2022) 631–633.
[35] K. Balaji, G.J.J. Wessley, Studies on the enhancement of aerodynamic performance in aerofoils using co-flow jet: a comprehensive review, Aerosp. Syst. 6 (1) (2023) 1–14.
[36] K. Xu, Y. Ren, G.-C. Zha, Separation control by co-flow wall jet, in: AIAA AVIATION 2021 Forum, 2021, p. 2946.
[37] M. Gad-el-Hak, D.M. Sushnell, Separation control: review, J. Fluids Eng. 113 (1991) 5–30, https://doi.org/10.1115/1.2926497.
[38] D. Coles, Topics in Shear Flow, Unpublished, 2017.
[39] P. Spalart, S. Allmaras, A one-equation turbulence model for aerodynamic flows, in: 30th Aerospace Sciences Meeting and Exhibit, 1992, p. 439.
[40] A. Seifert, L.G. Pack, Active flow separation control on wall-mounted hump at high Reynolds numbers, AIAA J. 40 (7) (2002) 1363–1372, https://doi.org/10.2514/2.1796.
[41] B. Wang, B. Haddoukessouni, J. Levy, G.-C. Zha, Numerical investigations of injection-slot-size effect on the performance of coflow jet airfoils, J. Aircr. 45 (6) (2008) 2084–2091.
[42] G.-C. Zha, E. Bilgen, Numerical solutions of Euler equations by using a new flux vector splitting scheme, Int. J. Numer. Methods Fluids 17 (2) (1993) 115–144.
[43] Y.-Q. Shen, G.-C. Zha, Improvement of the weno scheme smoothness estimator, Int. J. Numer. Methods Fluids 64 (6) (2010) 653–675.
[44] G.-C. Zha, Y.-Q. Shen, B. Wang, An improved low diffusion e-cusp upwind scheme, Comput. Fluids 48 (1) (2011) 214–220.

[45] G.-C. Zha, E. Bilgen, Numerical study of three-dimensional flows using unfactored upwind-relaxation sweeping algorithm, J. Comput. Phys. 125 (2) (1996) 425–433.
[46] X. Chen, G. Zha, Fully coupled fluid–structural interactions using an efficient high resolution upwind scheme, J. Fluids Struct. 20 (8) (2005) 1105–1125.
[47] K. Xu, G. Zha, Distortion elimination for serpentine inlet using CoFlow jet flow control with variation of Mach numbers, in: AIAA Propulsion and Energy 2020 Forum, 2020, p. 3775.
[48] K. Xu, G. Zha, Enhancing aircraft control surface effectiveness by co-flow jet flap at low energy expenditure, Aerosp. Sci. Technol. (2023) 108145.
[49] K. Xu, Y. Ren, G. Zha, Numerical investigation of NASA hump using co-flow jet for separation control, in: AIAA Scitech 2020 Forum, 2020, p. 1058.
[50] D. Greenblatt, K.B. Paschal, C.S. Yao, J. Harris, N.W. Schaeffler, A.E. Washburn, Experimental investigation of separation control part 1: baseline and steady suction, AIAA J. 44 (12) (2006) 2820–2830.
[51] D. Borgmann, A. Pande, J. Little, R. Woszidlo, Experimental study of discrete jet forcing for flow separation control on a wall mounted hump, in: 55th AIAA Aerospace Sciences Meeting, 2017, p. 1450.
[52] C. Rumsey, 2DWMH: 2D NASA Wall-Mounted Hump Separated Flow Validation Case, Turbulence Modeling Resource, 2003, turbmodels.larc.nasa.gov.
[53] R. Fisher, T. Nishino, M. Savill, Numerical analysis of a bidirectional synthetic jet for active flow control, AIAA J. 55 (3) (2017) 1064–1069.
[54] J.W. Naughton, S. Viken, D. Greenblatt, Skin friction measurements on the NASA hump model, AIAA J. 44 (6) (2006) 1255–1265, https://doi.org/10.2514/1.14192.
[55] K. Kara, D. Kim, P.J. Morris, Flow-separation control using sweeping jet actuator, AIAA J. 56 (11) (2018) 4604–4613.
[56] G. Tang, R.K. Agarwal, Numerical simulation of flow control over NASA hump with uniform blowing jet and synthetic jet, in: 2018 Flow Control Conference, 2018, p. 4017.
[57] P. Poisson-Quinton, L. Lepage, Survey of French Research on the Control of Boundary Layer and Circulation, Boundary Layer and Flow Control, vol. 1, 1961, pp. 21–73.
[58] F. Capizzano, P. Catalano, C. Marongiu, P.L. Vitagliano, U-rans modelling of turbulent flows controlled by synthetic jets, in: 35th AIAA Fluid Dynamics Conference and Exhibit, 2005, p. 5015.
[59] D. You, M. Wang, P. Moin, Large-eddy simulation of flow over a wall-mounted hump with separation control, AIAA J. 44 (11) (2006) 2571–2577.
[60] B. Dano, D. Kirk, G.-C. Zha, Experimental investigation of jet mixing mechanism of co-flow jet airfoil, in: 5th AIAA Flow Control Conference, 2010, p. 4421.
[61] K. Xu, G. Zha, Distortion elimination for serpentine duct at various Mach numbers using co-flow jet active flow control, Aerosp. Sci. Technol. 144 (2024) 108776.
[62] K. Xu, G. Zha, Mitigation of serpentine duct flow distortion using coflow jet active flow control, in: AIAA AVIATION 2020 Forum, 2020, p. 2954.
[63] A. Lefebvre, B. Dano, W.B. Bartow, M. Difronzo, G.-C. Zha, Performance and energy expenditure of coflow jet airfoil with variation of Mach number, J. Aircr. 53 (6) (2016) 1757–1767.
[64] H. Schlichting, K. Gersten, Boundary-Layer Theory, Springer–Verlag, 2001.